Journal of Applied Physics

Precision defect engineering of metal/insulator/metal diodes using atomic layer deposition to localize Ni impurities in Al_2O_3 tunnel barriers

Cite as: J. Appl. Phys. **129**, 144502 (2021); https://doi.org/10.1063/5.0045721
Submitted: 28 January 2021 . Accepted: 24 March 2021 . Published Online: 12 April 2021

Konner E. K. Holden, Yitong Qi, and John F. Conley

Journal of Applied Physics ARTICLE scitation.org/journal/jap

Precision defect engineering of metal/insulator/metal diodes using atomic layer deposition to localize Ni impurities in Al_2O_3 tunnel barriers

Cite as: J. Appl. Phys. **129**, 144502 (2021); doi: 10.1063/5.0045721
Submitted: 28 January 2021 · Accepted: 24 March 2021 ·
Published Online: 12 April 2021

Konner E. K. Holden, Yitong Qi,[a] and John F. Conley, Jr.[b]

AFFILIATIONS

School of Electrical Engineering and Computer Science, Oregon State University, Corvallis, Oregon 97330, USA

[a]**Present address:** Department of Chemistry and Chemical Biology, Harvard University, Cambridge, Massachusetts 02138, USA.
[b]**Author to whom correspondence should be addressed:** jconley@eecs.oregonstate.edu

ABSTRACT

Extrinsic impurity defect engineering is demonstrated to increase the maximum asymmetry of metal/insulator/metal (MIM) tunnel diodes. Using atomic layer deposition, transition metal Ni impurities are inserted at precise physical locations within the thickness of the insulating tunnel barrier in asymmetric electrode TiN/Al_2O_3/Al MIM diodes. The presence of Ni in Al_2O_3 is found to suppress the onset of Fowler–Nordheim tunneling from the Al electrode without changing the relative dielectric constant or refractive index of the insulator. Current–voltage asymmetry, a performance metric for MIM diodes, is reversed in Al_2O_3(Ni) devices and is increased over the control Al_2O_3 device (without Ni impurities) when the Ni impurities are placed close to the Al electrode. Capacitance–voltage measurements on MIM and metal/oxide/semiconductor devices along with Fowler–Nordheim derivative analysis all indicate the introduction of negative charge highly correlated with the position of the Ni defect layer within the Al_2O_3. Internal photoemission measurements show little change in zero-field energy barrier heights at the electrode interfaces, but varying field dependencies with respect to the position of the Ni defect layer. Combined results suggest that the level of the deep states introduced by the Ni atoms in Al_2O_3 is consistent with DFT predictions for the corundum Al_2O_3 system. Overall, this work demonstrates the possibility of improving MIM diode performance using precisely placed extrinsic defects.

I. INTRODUCTION

RECtifying anTENNA (rectenna) based infrared energy harvesting is being pursued as a method of reclaiming a large amount of the Sun's energy that is reradiated by Earth into space as heat as well as potentially recycling industrial waste heat back into usable electrical energy, a relatively untapped resource making up nearly 20%–50% of industrial energy input.[1] One of the major obstacles to achieving high efficiency THz rectennas is the rectifying diode. Thin film metal/insulator/metal (MIM) diodes, which operate on the principle of quantum tunneling, have received considerable attention for this and other ultra-fast rectifying applications such as THz detection.[2–5] Additionally, the simple architecture of MIM diodes facilitates integration into the back-end-of-line (BEOL) of integrated circuits so that they have already found application as protection diodes for mitigation of plasma-induced process damage and selector diodes for resistive random-access memory (RERAM). The possibility of integration on temperature sensitive substrates also makes them attractive for liquid crystal display backplanes and flexible electronics for large area energy harvesting arrays.

Key figures of merit for energy harvesting rectification include low turn-on voltage (V_{ON}) and high current (I) vs voltage (V) or current density (J) vs electric field (ξ) asymmetry ($f_{asym} = J^-/J^+$) and non-linearity [$f_{NL} = (dJ/dV)/(J/V)$]. The conventional method of producing high f_{asym} in MIM structures is to use metal electrodes with dissimilar work functions (Φ_M) to induce an equilibrium built-in voltage (V_{bi}) across the insulator and thus create an asymmetric tunnel barrier with enhanced Fowler–Nordheim tunneling (FNT) from the lower Φ_M electrode under forward bias. However, MIM diode performance using this method is restricted by the limited work function range of practical metal electrodes, as well as the choice of the single insulator.[6] Wide bandgap (E_G) insulators, though typically better suited for tunneling, have higher zero

bias resistance and higher V_{ON}. Narrow E_G insulators will typically result in lower V_{ON}, but conduction is often dominated by defect-related mechanisms and thus they are potentially problematic for high-speed operation and temperature stability. The trade-off between the choice of wide or narrow E_G insulators has recently been addressed by combining the two to form nanolaminate bi-layer insulator tunnel barrier MIIM diodes.[7–17]

For MIIM diodes in which conduction in both insulators is dominated by quantum mechanical tunneling, enhancements in f_{asym}, f_{NL}, and V_{ON} have been achieved via resonant tunneling and "step tunneling." In resonant tunneling, electrons under forward bias tunnel via FN through the narrow E_G insulator into quantum well states formed between the two insulators before tunneling via FN through the wide E_G insulator, while under reverse bias, electrons must tunnel through both barriers.[7,8,11] In step tunneling, electrons under forward bias tunnel directly through the wider E_G insulator into the conduction band of the narrower E_G insulator, while under reverse, bias they also must tunnel through both insulators.[9] In both cases, lower V_{ON} and higher f_{asym} and f_{NL} may be achieved over single insulator MIMs of similar thicknesses.[8–10,12,13,15,16,18] A number of MIIM insulator and electrode combinations have been explored, as well as other rectification enhancement approaches, including additional insulators (MIIIM, etc.),[13,16,17,19] graded insulators,[20] and geometry enhancement through the use of patterned electrodes, CNTs, and graphene.[13,16,18,21–25]

A more novel approach to MIIM diodes takes advantages of deep-level defects. For MIIM diodes in which the narrow E_G insulator contains *intrinsic* defects that contribute to bulk conduction, f_{asym} at low V_{ON} may be further improved via "defect-enhanced direct tunneling" (DEDT), in which under forward bias electrons may transport easily across the narrow E_G insulator via intrinsic defect-enhanced (DE) Frenkel–Poole emission before direct tunneling (DT) through an adjacent wider E_G insulator.[10] Under reverse bias, electrons must first tunnel through the wide E_G insulator. The wide E_G layer thus ensures that operation is limited by tunneling, reducing temperature dependence. Although this method has been demonstrated to improve rectification, it is limited by the lack of precise control over the density, spatial distribution, and energy levels of the intrinsic defects in the narrow E_G insulator.

Despite extensive work, the performance achieved to date on various MIM diodes (and extensions thereof) is still not sufficient for rectenna applications. A new approach is required. Herein, we expand upon the DEDT approach. We propose a defect engineering strategy that involves the intentional placement of *extrinsic* impurities to introduce allowed energy states at desirable levels and at precise physical positioning within the bandgap of the tunnel barrier. The anticipated mechanism for rectification improvement is based on asymmetric trap-assisted tunneling (TAT) conduction, as schematically illustrated in Fig. 1 for defects with states above the equilibrium Fermi energy. When extrinsic defect states become aligned with the emitting electrode Fermi level, electrons may tunnel into the defects before tunneling onto the opposite electrode, effectively increasing tunneling probability and resulting in a sharp increase in current at lower voltages. The polarity at which the defect states align with the emitting electrode at a lower magnitude voltage is considered forward bias. Under reverse bias at the same magnitude voltage but opposite polarity, the defect levels do not align with emitting electrons and the electrons must tunnel through the entire barrier. The physical location of the defects is important. When the defects are located nearer the smaller work function electrode, as illustrated in Fig. 1(a), the asymmetry induced by the defects opposes the built-in asymmetry induced by the dissimilar work function electrodes and may, therefore, reduce the magnitude or even reverse the polarity of the asymmetry. In this case, the reversed asymmetry could be higher than for devices without defects but would likely occur at a higher V_{ON}. However, when the defects are physically located nearer the large work function electrode, as illustrated in Fig. 1(c), the asymmetry induced by the defects is in the same direction as the built-in asymmetry induced by dissimilar work function electrodes and has the

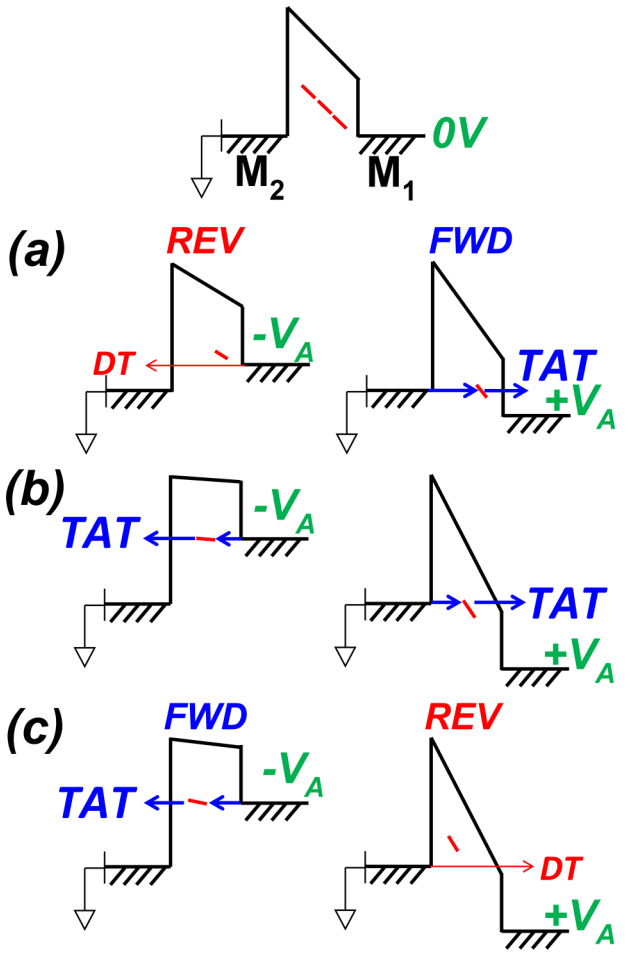

FIG. 1. Band diagrams illustrating the envisioned TAT enhanced conduction process for defects intentionally placed (a) near the low work function electrode, (b) in the middle of the tunnel barrier, and (c) near the high work function electrode. An equilibrium zero bias band diagram is provided at the top of the figure. The defect energy level (red dash) is fixed at the same energy offset with respect to the insulator conduction band for all three configurations. For each configuration, the same magnitude positive and negative applied bias is used.

potential to enhance asymmetry at reduced V_{ON}, critical for rectenna applications. Finally, defects placed in the middle of the tunnel barrier, as in Fig. 1(b), would likely have less of an impact on maximum asymmetry due to the alignment voltage being the same for both polarities, but may still result in a reduction of V_{ON}.

In this work, we employ atomic layer deposition (ALD) to place Ni impurities at precise locations within an Al_2O_3 tunnel barrier in order to introduce defects with energy levels near the Fermi level of the metal electrodes. Ni was chosen based on a density functional theory (DFT) study of the energy levels introduced by transition metal impurities in the corundum Al_2O_3 system.[26] Ni is predicted to introduce defect levels at roughly 2 eV above the Al_2O_3 valence band maximum—near the Fermi levels of both the TiN and Al electrodes used in this work. The impact of Ni impurities as a function of position in the Al_2O_3 insulating layer is investigated using (J–ξ) measurements of MIM devices and capacitance vs voltage (C–V) measurements of MIM and metal/oxide/semiconductor (MOS) devices. Internal photoemission (IPE) spectroscopy is performed to examine the influence of Ni impurities on the metal electrode/Al_2O_3 electron energy barriers.

II. EXPERIMENTAL

MIM diodes and MOS capacitors were fabricated by depositing Al_2O_3(Ni) films onto either Si/SiO_2/Ti/TiN substrates (provided by ON Semiconductor) or directly on RCA cleaned n^+ Si ($N_D = 10^{18}$ cm^{-3}). Chemical mechanical polishing of the TiN reduced roughness to 0.4 nm RMS, low enough to minimize background conduction due to electrode roughness (geometrical) electric field enhancement.[27] ALD of Al_2O_3 and Ni impurity defect layers were carried out in a Picosun SUNALE R-150B reactor at 200 °C and ~100 mTorr using alternating N_2-purge-separated pulses of either trimethylaluminum (TMA) and H_2O or Ni(^{tBu2}DAD)$_2$ and O_3/O_2,[28] respectively. O_3 was generated using an IN-USA AC-2025 ozone generator operated at 50% power, yielding an expected O_3/O_2 concentration of ~10%. TMA was kept at room temperature, while Ni(^{tBu2}DAD)$_2$ was heated to 150 °C and delivered by a Picosun PicoSolid Booster source. Ni impurities were placed inside a baseline 10 nm thick Al_2O_3 barrier by interrupting the 100-cycle Al_2O_3 deposition sequence with two ALD cycles of Ni(^{tBu2}DAD)$_2$ and O_3 without breaking vacuum. The "bulk" growth per cycle (GPC) of the TMA/H_2O and Ni(^{tBu2}DAD)$_2$/O_3 processes were 0.10 and 0.12 nm/cycle, respectively. The thickness and refractive index (RI) of Al_2O_3 and Al_2O_3(Ni) films deposited on Si substrates with a ~1.6 nm native SiO_2 layer was measured using a Woollam M-2000 variable-angle spectroscopic ellipsometer (VASE) in the wavelength range of 300–1000 nm and modeled using the Cauchy dispersion formula. Thicknesses determined by VASE were used in electric field calculations for the corresponding Al_2O_3 or Al_2O_3(Ni) MIM diodes.

Following insulator deposition, TiN/Al_2O_3(Ni) and Si/Al_2O_3(Ni) samples were transferred to a high vacuum deposition chamber where ~100 nm Al was thermally evaporated at a base pressure of 3×10^{-6} Torr through circular shadow masks with radii of ~75, ~125, and ~250 μm to form top electrodes and complete formation of MIM and MOS devices. The area of the top electrodes was measured with an optical microscope and used for area normalizations. I–V and C–V measurements were taken using a probe station in a dark box with an Agilent B1500A semiconductor parameter analyzer and E4980A LCR meter, respectively.

Five different device types were prepared, featuring a baseline Al_2O_3 film and four Al_2O_3(Ni) films. The Al_2O_3(Ni) devices are labeled *Bottom* for the Ni defect layer placed closest to the bottom TiN electrode with 25/2/75 cycles of Al_2O_3/Ni defects/Al_2O_3, *Middle* for Ni placed equidistant between both electrodes (50/2/50), *Top* for Ni placed closest to the top Al electrode (75/2/25), *Doped* for Ni placed uniformly throughout the film (25/2/25/2/25/2/25), and *Control* for the 100-cycle baseline Al_2O_3 film. Schematic cross sections in Fig. 2(a) illustrate Ni positioning. As two cycles of Ni(^{tBu2}DAD)$_2$/O_3 are expected to deposit less than a full monolayer of material, dashed lines are used to indicate the discontinuous nature of the Ni incorporation. [This is consistent with a high-resolution transmission electron microscope cross-sectional image, seen in Fig. S1 in the supplementary material, of the *Doped* device in which no distinct layers or islands within the Al_2O_3 attributable to the addition of Ni(^{tBu2}DAD)$_2$/O_3 pulses could be resolved.] Corresponding band diagrams in Fig. 2(b) show the estimated spatial and energetic[26] location of the Ni defect states, using the metal/Al_2O_3 barrier heights measured on the baseline *Control* system with IPE and the bandgap of Al_2O_3 measured using reflected electron energy loss spectroscopy, both from our previous work[6,29] and Afanas'ev *et al.*[30]

Metal/insulator electron energy barrier heights were determined using IPE. IPE measurements were conducted on a home-built system using light from a 150 W Xe arc lamp source that was passed through a monochromator and then a long-pass filter (to remove second-order diffraction) before being focused on the device. Electrical bias was applied to the bottom electrode and the top electrode was held at ground. At each applied voltage bias, the electrical current was measured as the photon energy ($h\nu$) was swept from 2 to 5 eV (620–248 nm). The quantum yield, Y, was calculated from normalized current. IPE spectral thresholds φ_{thresh}, the photon energy at which photoinduced current exceeds the dark current for a given applied bias, were determined from plots of $Y^{1/2}$ vs $h\nu$.[31,32] The zero-field barrier height, φ_{Bn}, for each metal/Al_2O_3 interface was then determined by taking the y-intercept of a

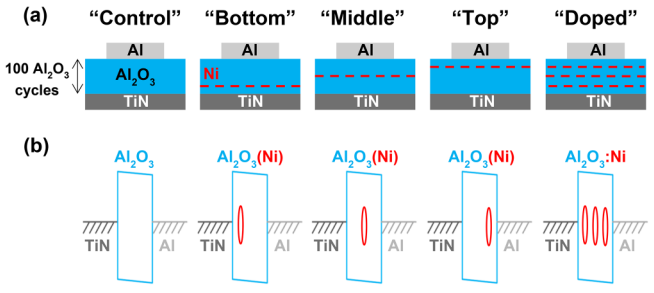

FIG. 2. (a) Schematic cross sections of TiN/Al_2O_3/Al MIM diodes showing placement of Ni defect layers (red dashed lines) and naming scheme. (b) Predicted energy band diagrams for the device structures shown in (a) with estimated distributions of Ni defect state energies and locations (red ovals).

Schottky plot of φ_{thresh} vs the square root of the insulator electric field, $\xi_{ox}^{1/2}$, with an estimated accuracy of ±0.1 eV.[30] The $\xi_{ox}^{1/2}$ values are corrected for the built-in field of each device, $|\xi_{ox}|^{1/2} = |(V_{bias} - \Delta\phi_M)/d_{ox}|^{1/2}$. The voltage at which photocurrent changes polarity is taken as the built-in potential, i.e., the work function difference, $\Delta\phi_M$. Further details about the system and barrier analysis may be found in our earlier work using the same IPE system.[33]

III. RESULTS AND DISCUSSION

A. Film characterization

Films were initially characterized using VASE to determine if the introduction of the two Ni(^{tBu2}DAD)$_2$/O$_3$cycles significantly altered the thickness or refractive index (RI), i.e., the macroscopic properties of the material. The thickness of Al_2O_3(Ni) films deposited on Si witness coupons, shown in Fig. 3(a), is increased slightly with the addition of these cycles. The nominal 10 nm thickness of the baseline 100-cycle Al_2O_3 process increases by an average of $\Delta d_{ox} = 0.6$ nm for the *Bottom, Middle,* and *Top* devices, and by $\Delta d_{ox} = 1.8$ nm for the *Doped* device. Though Δd_{ox} is higher than expected based on the NiO process growth-per-cycle of 0.12 nm/cycle,[28] the incorporation of Ni or the use of the more aggressive O_3 may enhance growth during the subsequent initial cycles of the TMA/H_2O Al_2O_3 process. Figure 3(b) plots refractive index (RI) and mean standard error (MSE), fitted using a Cauchy dispersion model, for the same films. The RI of 1.67 for the *Control* film was relatively unchanged by Ni incorporation for the films studied in this work. An additional film with two Ni (^{tBu2}DAD)$_2$/O$_3$ cycles for every 10 Al_2O_3 cycles [10/(2/10) × 9] showed a slightly higher RI of 1.7 and a slightly larger deviation, potentially indicating a more uniform composition ternary Ni_xAl_yO film.[34] The electrical response of this latter device was not studied in this work as it is not expected to exhibit the intended trap-assisted conduction nor possibly even insulating behavior. For the other devices, the consistent RI and MSE together indicate that the addition of Ni(^{tBu2}DAD)$_2$/O$_3$ pulses has not significantly affected the macroscopic properties of the film.

B. Identification of conduction mechanisms

Representative room temperature logarithmic *J*–*ξ* sweeps of Al_2O_3 MIM devices with and without Ni impurities are shown in Fig. 4(a). The voltage applied to the top Al electrode was swept continuously from 0 V to positive voltage, then to negative voltage, then back to 0 V. To stabilize the devices, this voltage sweep is repeated for five times. The fifth sweep is then used for comparison. (Figure S2 in the supplementary material shows plots of multiple overlaid time zero dielectric breakdown *I*–*V* curves. Good repeatability is seen among the 15–17 individual devices measured for each polarity for each device type, with little variation in breakdown strength between the various device types, shown in Fig. S2 in the supplementary material.) At low *ξ*, all of the Al_2O_3(Ni) devices show nearly an order of magnitude higher *J* than the *Control* Al_2O_3 device. The elevated leakage at low electric field for all Al_2O_3(Ni) devices is an indication of defect conduction due to the incorporation of Ni impurities. The immediate onset of this elevated leakage at both polarities suggests that the Ni defect energy levels lie close to or just below the electrode Fermi levels, consistent with DFT calculations.[26]

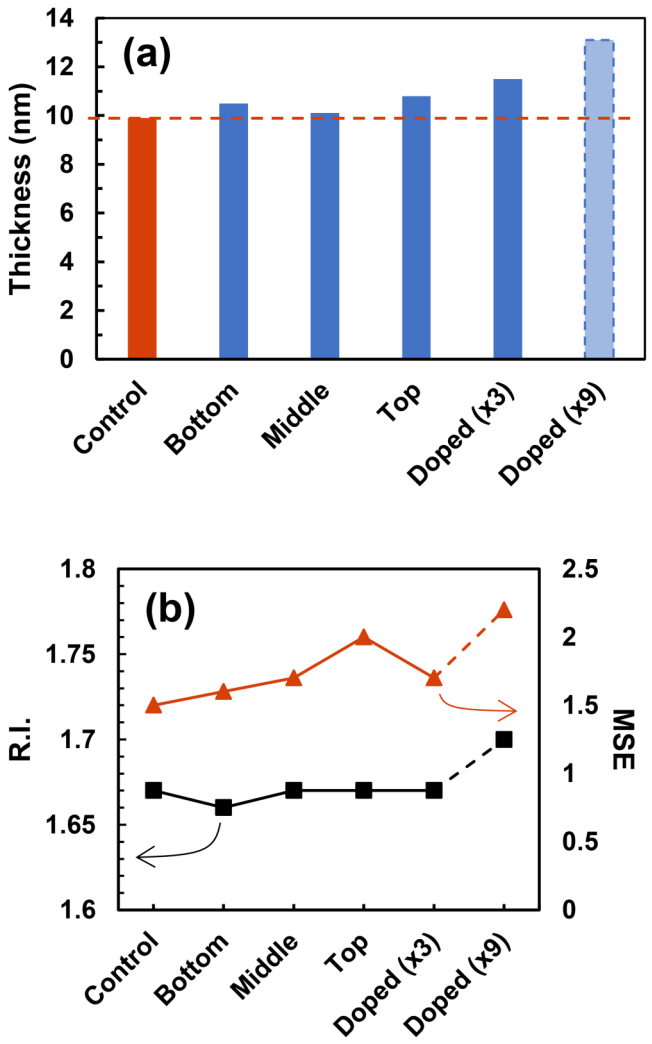

FIG. 3. Plot of ellipsometric (a) Al_2O_3 (orange) and Al_2O_3(Ni) (blue) film thickness vs device structure and (b) RI and MSE, measured using a bare Si witness coupon. The orange dashed horizontal line in (a) indicates the thickness of the Control 100-cycle Al_2O_3 film for ease of comparison. The "Doped (×9)" device, plotted with dashed lines in (a) and (b), was excluded from further study in this work.

As *ξ* increases, the sharp increases (or "knees") in *J* near −2.5 and +3 MV/cm for the *Control* device indicate the onset of FNT conduction. The *Bottom*, *Middle*, and *Top* Al_2O_3(Ni) devices also exhibit sharp increases in current at both polarities, though in some cases less sharp than for the *Control* device. For positive polarity, the onset of the *J* knee is nearly the same for all devices. For negative polarity (electron injection from the Al electrode), however, the knee occurs at higher magnitude *ξ* for the *Bottom*, *Middle*, and *Top* Al_2O_3(Ni) devices. The *Doped* device exhibits a large symmetric

increase in leakage with less distinct knees occurring at reduced ξ. Though the sharp increase in J at higher ξ for the *Bottom and Top* devices is likely due to FNT, the suppressed onset at negative polarity (injection from top Al electrode) and marked slope change for the *Middle*, *Top*, and *Doped* devices suggest the presence of negative charge associated with the Ni impurities.

f_{asym}–ξ curves are shown in Fig. 4(b). The *Control* Al_2O_3 device shows $f_{asym} > 1$, beginning at about $\xi = 2.5$ MV/cm and saturating at approximately $f_{asym,max} = 26$. The Al_2O_3(Ni) devices show weak to strong *reversal* of asymmetry to $f_{asym} < 1$. The symmetric *Middle* and *Doped* Al_2O_3(Ni) devices show a weak reversal of asymmetry and nearly symmetric J–ξ response with f_{asym} close to unity. The asymmetrically modified *Bottom* and *Top* Al_2O_3(Ni) devices, with Ni introduced near one or the other electrodes, show strongly reversed asymmetry. For the *Top* device, $f_{asym,max} = 4.2 \times 10^{-3}$ ($f_{asym,max}^{-1} = 240$) at high ξ, nearly an order of magnitude higher than the *Control* device. The voltage onset of asymmetric operation, V_{ON}, is increased in both *Bottom* and *Top* devices. Thus, the improved $f_{asym,max}$ is due to the suppression of the onset of negative polarity FNT (especially in the *Top* device), rather than an increase in positive polarity conduction, as was desired. Potential reasons for the suppressed onset of FNT (and V_{ON}) include the increased pre-FNT background defect assisted conduction, negative trapped charge associated with the Ni impurities, and, possibly, negative charge induced increase of the Al electrode φ_{Bn}.

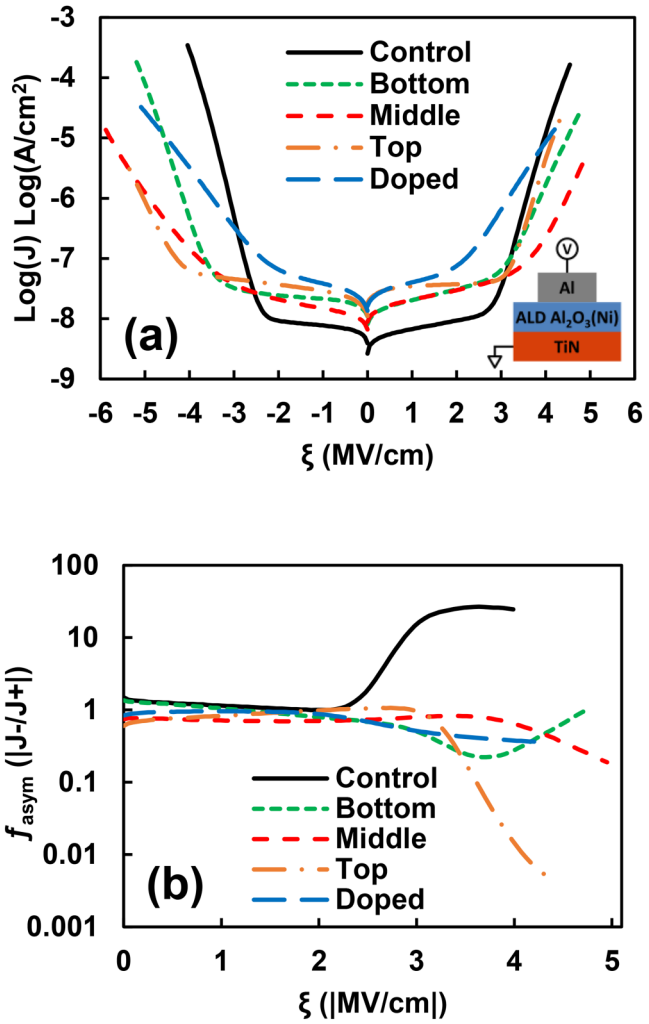

FIG. 4. (a) Logarithmic J–ξ sweeps and (b) corresponding f_{asym}–ξ data for TiN/Al_2O_3/Al MIM diodes without (solid black line) and with (dashed lines) intentionally placed Ni impurities. Data are recorded after the fifth sweep.

C. MIM and MOS capacitance–voltage characteristics

To elucidate the presence and effect of charge within the tunnel barrier, C–ξ sweeps were performed on the same MIM devices from Fig. 4 as well as MOS devices with dielectrics deposited in the same ALD run. Shown in Fig. 5(a) are C–ξ plots normalized to the zero-field capacitance, C_0. Data are recorded after the second sweep. All devices exhibit a non-linear dependence of capacitance on ξ, which is widely reported for MIM devices.[35–37] This field dependence of capacitance is empirically described by $C(\xi)/C_0 = \alpha\xi^2 + \beta\xi + 1$, and α and β are the quadratic and linear coefficients of capacitance, respectively. The α values and relative dielectric constants, κ (calculated from $\kappa = C_0 d_{ox}/\epsilon_0 A$) do not differ significantly among the devices (500 ± 21 ppm/ξ^2 and 8.2 ± 0.2, respectively) and are within the range of similar MIM devices,[37] indicating that the introduction of Ni impurities has little effect on macroscopic or "bulk" dielectric behavior. The ξ at minimum capacitance, $\xi(C_{min})$, is plotted in Fig. 5(b). $\xi(C_{min})$ is shifted to more positive ξ for the Al_2O_3(Ni) devices, particularly for the devices with Ni close to the Al electrode. Besset *et al.* have suggested that shifts in $\xi(C_{min})$ are linked to the presence of charge in the insulator, analogous to the flatband voltage shift (ΔV_{FB}) for MOS CV curves.[38] The positive shift in $\xi(C_{min})$ in the Al_2O_3(Ni) devices, therefore, could indicate the presence of negative charge. The largest magnitude of $\xi(C_{min})$ shift is observed in the *Top* and *Doped* devices in which the Ni impurities are located either next to the Al electrode or distributed throughout the Al_2O_3 dielectric.

Shown in Fig. 6(a) are C–V curves for Al/Al_2O_3/Si pMOS capacitors, where V is first swept positive and then negative, starting from −3 V. Data are recorded after the second full sweep. ΔV_{FB} from the ideal $V_{FB} = \phi_{MS}$ (where ϕ_{MS} is the metal–semiconductor work function difference) are plotted in Fig. 6(b). ΔV_{FB} is taken using the inflection point method and the average of the positive and negative sweeps.[39] The *Control* device exhibits a slight negative ΔV_{FB}, indicating the presence of positive charge for the baseline ALD Al_2O_3 film. A positive ΔV_{FB} is observed for all of the Al_2O_3(Ni) devices, increasing as the Ni defect layer is introduced closer to the Si substrate, providing further evidence of Ni-associated negative charge in the Al_2O_3. Voltage hysteresis is seen in all devices between positive and negative sweeps with increased hysteresis in the Al_2O_3(Ni) devices. Since the underlying Si was cleaned using the same RCA procedure for all MOS devices, there are expected to be few extrinsic impurities at the Si/Al_2O_3 interface, suggesting that the hysteresis is likely related to switching traps in the bulk of insulator. The magnitude of the hysteresis

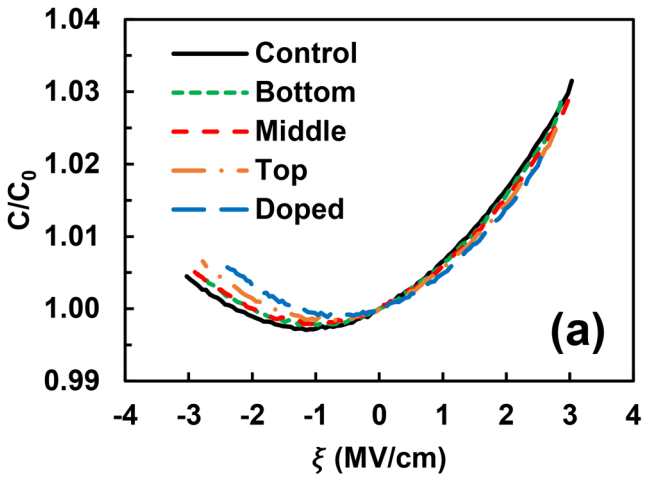

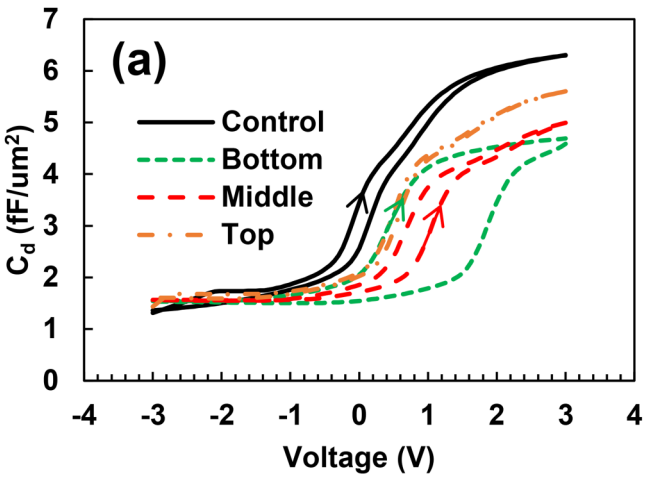

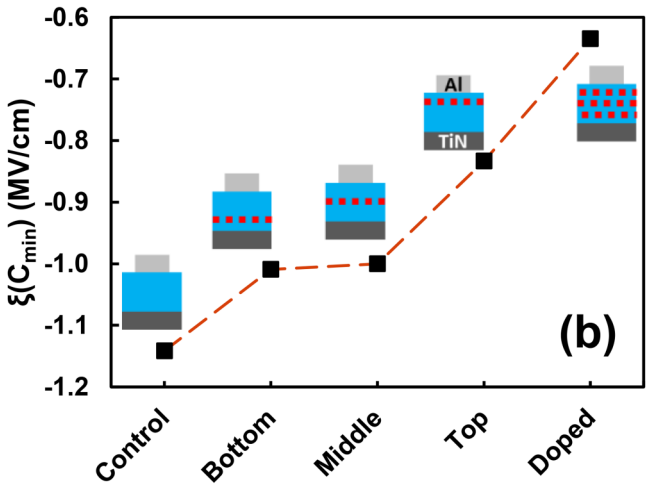

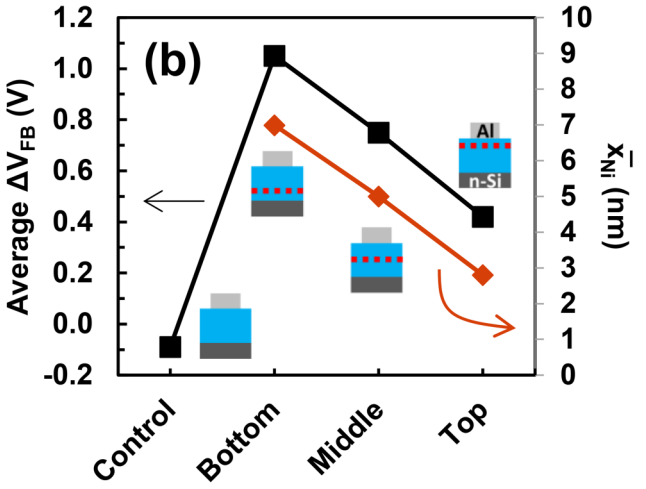

FIG. 5. Normalized C/C_0 vs ξ for $TiN/Al_2O_3/Al$ and $TiN/Al_2O_3(Ni)/Al$ MIM devices. (b) Electric field at minimum capacitance taken from (a) with inset device cross sections indicating intended Ni impurity placement.

FIG. 6. (a) *C–V* curves for Al_2O_3 (solid line) and $Al_2O_3(Ni)$ (dashed lines) pMOS devices with sweep directions indicated by arrows. (b) Plot of calculated average ΔV_{FB} and $\bar{x}_{Ni}$ values for the devices in (a).

increases as the Ni defects are placed closer to the Si substrate (further from the Al electrode). As charge trapped at defects closer to the Si substrate has a larger impact on hysteresis than charge trapped at defects further away, this suggests that the hysteresis may be due to charging and discharging of deep-level traps associated with the Ni impurities.

Using the sheet charge approximation at the distance of the Ni defect charge centroid from the top Al electrode, $\bar{x}_{Ni}$, and ignoring any interfacial charge, the flatband voltage equation,

$$V_{FB} = \phi_{MS} - \frac{1}{\kappa}\int_0^{t_{ox}} \rho(x)x\,dx, \tag{1}$$

where $\rho(x) = Q_{Ni}\delta(x - \bar{x}_{Ni})$ is the charge density distribution in the oxide and Q_{Ni} is the sheet charge density at $\bar{x}_{Ni}$, can provide an approximation for $\bar{x}_{Ni}$ by evaluating the integral on the right-hand side and rearranging so that

$$\bar{x}_{Ni} = (V_{FB} - \phi_{MS})\frac{\epsilon_r}{Q_{Ni}}. \tag{2}$$

Selecting the *Middle* device as a reference and fixing $\bar{x}_{Ni} = 5$ nm, the Ni defect charge density is calculated as $Q_{Ni} = -1.1 \times 10^{-6}$ C/cm^2 or 6.9×10^{12} trapped electrons/cm^2. The approximate charge centroid values for each device are plotted on the right-hand axis of Fig. 6(b). This qualitative assessment provides further

evidence that the Ni defect layers introduce negative charge and that they are positioned at the intended locations in the Al_2O_3 film.

D. Internal photoemission (IPE) spectroscopy: Determination of barrier heights

IPE spectroscopy was used to determine whether the Ni impurities have an impact on either of the metal/insulator barriers. Shown in Fig. 7 are representative IPE yield plots of $Y^{1/2}$ vs $h\nu$ for the *Control*, *Top*, and *Bottom* devices under (a) negative and (b) positive applied bias, corresponding to electron emission from the top Al or bottom TiN electrode, respectively. Values of φ_{thresh} are determined for each applied ξ_{ox} and may be subject to image force lowering, in which

$$\phi_{thresh}(\xi_{ox}) = \phi_{Bn} - \sqrt{\frac{q}{4\pi\epsilon_{opt}}}\sqrt{\xi_{ox}}, \tag{3}$$

where q is the electron charge in Coulombs and ϵ_{opt} is the optical dielectric constant of the oxide. To account for the presence of any image force lowering, the φ_{thresh} values are thus plotted vs the square root of the absolute value of the insulator field $|\xi_{ox}|^{1/2}$, shown in Figs. 7(c) and 7(d) for negative and positive bias, respectively. The φ_{Bn} value for each device is then obtained by linear extrapolation to zero field.

For the *Control* Al_2O_3 device, $\varphi_{Bn,Al}$ and $\varphi_{Bn,TiN}$ were found to be 3.1 ± 0.1 and 3.3 ± 0.1 eV, respectively, within error of previously

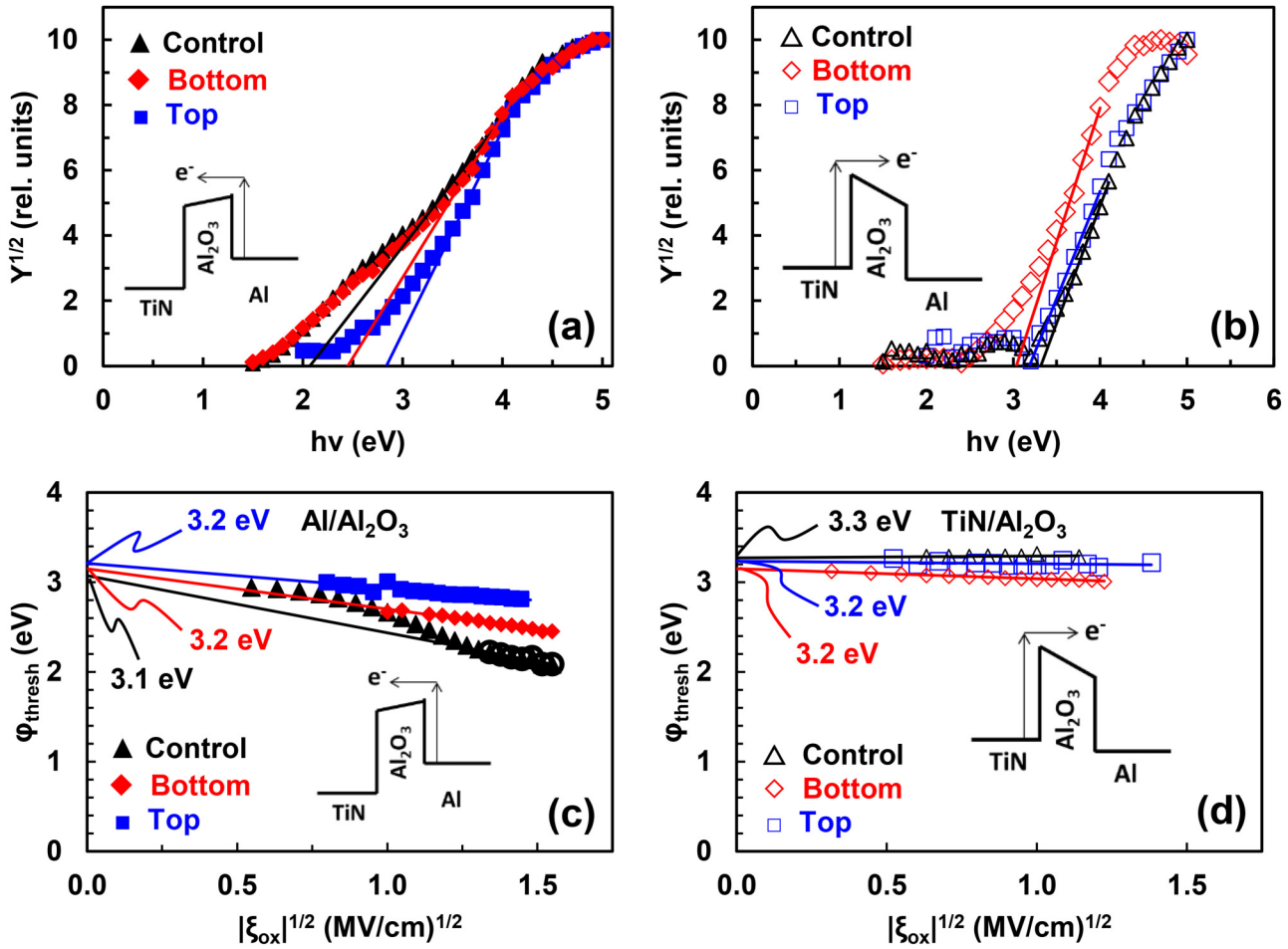

FIG. 7. Plots of IPE $Y^{1/2}$ vs $h\nu$ taken at (a) 1.4 $(MV/cm)^{1/2}$ for emission from the Al electrode and (b) 1 $(MV/cm)^{1/2}$ for emission from the TiN electrode. φ_{thresh} values are determined using the correspondingly colored linear regression lines. Inset band diagrams indicate the applied bias polarity and the direction of electron emission for each plot. IPE-derived Schottky plots of φ_{thresh} vs $|\xi_{ox}|^{1/2}$ for the *Control* (black) Al_2O_3 device, and *Bottom* (red) and *Top* (blue) Al_2O_3(Ni) devices for emission from the (c) Al and (d) TiN electrodes, with color-coded callouts to y axis-extrapolated φ_{Bn} values. High-field data points for the *Control* zero-field extrapolation in (c) are circled. All other extrapolations in (c) and (d) are carried out using the full dataset.

reported IPE values of 3.2 ± 0.1 eV for $\varphi_{Bn,Al}$[29,31] and estimates of 2.5–3.3 eV for $\varphi_{Bn,TiN}$ from FNT J–ξ analysis,[40,41] respectively. Note that whereas the $\varphi_{Bn,TiN}$ was extrapolated from the entire field range, $\varphi_{Bn,Al}$ was extrapolated from $\xi_{ox}^{1/2} > \sim 1.25$ $(\mathrm{MV/cm})^{1/2}$ (fitting data points are circled), similar to the field range used in the work by Jenkins *et al.*[29] Using an electron affinity of 1.4 eV for ALD Al_2O_3[42] places the work functions near expected values of 4.7 eV for TiN[43] and 4.4 eV for Al.[31,44]

For the *Bottom* Al_2O_3(Ni) device, in which the Ni impurities are introduced closer to the TiN electrode, it was found that $\varphi_{Bn,Al}$ was 3.2 ± 0.1 eV (within experimental error of the *Control* film), but with a substantial decrease in the Schottky slope [Fig. 7(c)]. The $Y^{1/2}$ vs $h\nu$ behavior for emission from Al, seen in Fig. 7(a), is nearly identical to the *Control* device. However, for the *Top* device with the Ni impurity layer introduced closer to the Al electrode, $\varphi_{Bn,Al}$ was also 3.2 ± 0.1 eV and within experimental error of the *Control* device, but with an even greater decrease in the Schottky slope. In addition, there was a marked change in the $Y^{1/2}$ curve of the *Top* device in Fig. 7(a). The disappearance of the low photon energy tail results in a sharper photoemission threshold, indicating a sharper energy barrier for which the charge screening effect of the Ni impurity may be responsible.

For emission from the TiN electrode, the $\varphi_{Bn,TiN}$ values and the Schottky slope for both the *Bottom* and *Top* devices are relatively unchanged as compared to the *Control* Al_2O_3 device [Fig. 7(d)]. The $Y^{1/2}$ curves [Fig. 7(b)] for all devices are also very similar in shape, which indicates that the barrier landscape near this interface remains largely unaffected. The TiN/high-κ oxide interface is expected to be highly stable and thus the effect of screening or image force barrier lowering is not readily observed,[43] as compared to the Al/Al_2O_3 interface.

IV. DISCUSSION

The strong dependence of FNT conduction on the placement of Ni in the Al_2O_3(Ni) devices [Fig. 4(a)] may be further analyzed. In the absence of charge at the interface or within the barrier, FNT conduction is described in the simplified form of

$$J_{FNT} = \frac{q^2\xi^2}{8\pi hq\varphi_{Bn}} \exp\left(-\frac{8\pi(2qm_T^* m_0)^{1/2}}{3h\xi}\varphi_{Bn}^{3/2}\right), \quad (4)$$

where q is the electron charge, h is the Planck constant, and m_T^* is the electron tunneling effective mass. In Fig. 8, the data from Fig. 4(a) are replotted as $\ln(J/\xi^2)$ vs $1/\xi$. Good ($R^2 > 0.995$) linear fits are obtained for both polarities for the asymmetric J–ξ behavior *Control*, *Bottom*, and *Top* devices indicating a dominant role for FNT conduction.

Manually fitting Eq. (4) to the *Control* Al_2O_3 device requires setting m_T^*=0.07, below the range of reported values of 0.16–0.45,[45,46] to yield $\varphi_{Bn,Al}$ and $\varphi_{Bn,TiN}$ estimates consistent with IPE measurements, 3.1 and 3.3 eV, respectively. Using m_T^*=0.07 for FNT fitting of the *Bottom* and *Top* devices results in poor fits and barrier heights estimates of $\varphi_{Bn,Al}$ ~3.5 and ~3.8 eV, respectively, and $\varphi_{Bn,TiN}$ = 3.5 eV for both, higher than those measured by IPE. The overestimation of barrier heights suggests either an increase in

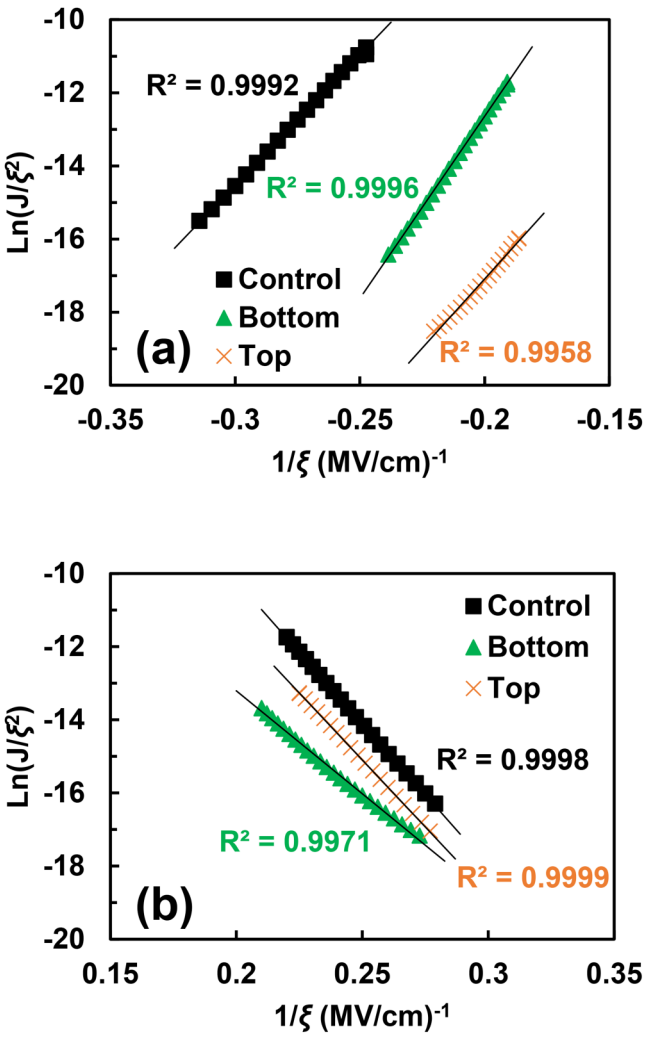

FIG. 8. (a) Negative and (b) positive bias FN plots of $\ln(J/\xi^2)$ vs $1/\xi$ taken after the J "knee" from the J–ξ curves of Fig. 4(a) for *Control*, *Bottom*, and *Top* devices with corresponding color-coded coefficient of determination (R^2) values. The *Middle* and *Doped* devices are excluded due to low R^2 values (<0.99).

m_T^* due to Ni incorporation or that trapped charge associated with the Ni impurities impacts the shape of the Al_2O_3 tunnel barrier. Taken together, the MIM J–ξ and C–ξ, MOS C–V, and IPE measurements all point toward the presence of negative charge in the Al_2O_3 associated with the introduction of the two Ni(^{tBu2}DAD)$_2$/O_3 cycles. Assuming little to no change in φ_{Bn}, as indicated by IPE, negative charge at the Ni defect centroid would cause localized upward bending of the Al_2O_3 bands, which would result in a non-triangular energy barrier, as depicted in Fig. 9. This non-triangular tunnel barrier is not accounted for by the simplified form of FNT given in Eq. (4) and is the likely cause of the poor fits and inaccurate approximations of φ_{Bn}.

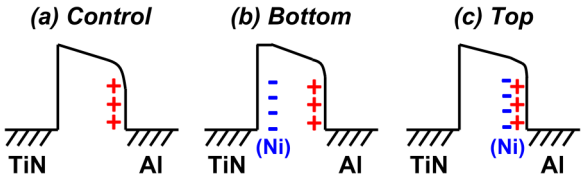

FIG. 9. Band diagrams illustrating the impact of Ni-associated negative charge (blue minus signs) in the (a) *Control*, (b) *Bottom*, and (c) *Top* devices. Positive charge (red plus signs) in the as-deposited Al_2O_3 film is shown at the Al interface.

The Fowler–Nordheim derivative (*FND*) method has been proposed to assess the evolution of injected charge during gate stress in MOS devices[47] and is described as

$$FND(\xi) = \partial \ln (J/\xi_{ox}^2)/\ \partial(1/\xi_{ox}). \tag{5}$$

Kies *et al.*[47] note that both the magnitude and curvature of *FND* vs ξ plots reveal certain aspects of the charge density as well as the centroid position within the tunnel barrier. The magnitude of the peak *FND* value is more closely related to charge density, while ξ at the peak value is influenced more by the centroid position. However, it should be noted that the density and centroid position using this approach are conflated with each other as well as with the φ_{Bn} of the injecting electrode.[47] Even assuming that φ_{Bn} remains mostly unchanged, as indicated by IPE measurements, the FND method is not meant as a quantitative assessment of charge density and centroid location. Rather, the FND method provides a qualitative connection of the J–ξ curves to trapped charge within the insulator. Shown in Fig. 10 is a plot of the *FND* vs ξ for the negative bias (injection from Al) J–ξ curves from Fig. 4(a) for the

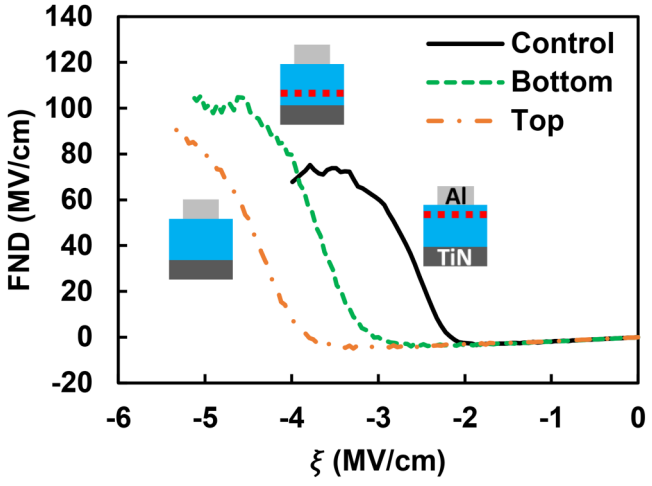

FIG. 10. *FND* vs ξ for the *Control* TiN/Al_2O_3/Al and the *Top* and *Bottom* TiN/Al_2O_3(Ni)/Al devices.

Control, *Bottom*, and *Top* devices. In the FNT regime of operation (> |3 MV/cm|), the *FND*–ξ curve of the *Control* device shows a rough saturation plateau at ~75 MV/cm at $\xi < -3.25$ MV/cm, indicating the onset of the "true" FNT conduction region, consistent with Fig. 8(a). The *Bottom* device reaches a larger maximum of about 105 MV/cm at $\xi < -4.5$ MV/cm, suggesting increased negative charge density relative to the *Control* device. While not reaching a saturation plateau (due to being cut off at more than an order of magnitude lower current than the *Bottom* device), the FND curve for the *Top* device behaves similarly and is shifted parallel by about −1 MV/cm toward more negative ξ. This suggests that $\bar{x}_{Ni}$ of the negative charge is located closer to the Al electrode. A rough quantitative assessment can be performed using the formulation from Kies *et al.*[47] for

$$\bar{x}_{Ni} = \frac{\varphi_{Bn,Al}}{\xi_{ox,m}}\left(2 - \sqrt{D_0/D_m}\right), \tag{6}$$

and

$$Q_{Ni} = \left(\sqrt{D_0/D_m} - 1\right)\frac{\epsilon_r \epsilon_0 \varphi_{Bn,Al}}{\lambda(1-\lambda)t_{ox}}, \tag{7}$$

where $\xi_{ox,m}$ is the applied electric field at the maximum FND value D_m, D_0 is the FND maximum value for the *Control* device, and $\lambda = \bar{x}_{Ni}/t_{ox}$. Using Eqs. (6) and (7), estimates of $\bar{x}_{Ni}$ of 7.9 and 6.0 nm, with Q_{Ni} of -7.5×10^{-6} and -8.9×10^{-6} C/cm^2 (4.7×10^{13} and 5.6×10^{13} trapped electrons/cm^2 respectively), are obtained for the *Bottom* and *Top* devices, respectively. The values for Q_{Ni} and trend of $\bar{x}_{Ni}$ using the FND approach, while only rough approximations are consistent the MOS ΔV_{FB}-based estimates provided earlier and point to negative charge associated with the Ni impurity centroid.

Although determining more precisely the density and position of the trapped charge would require an extensive modeling effort, MOS and MIM C–V measurements and *FND* analysis all indicate that the negative charge appears to be highly correlated with the location of the Ni ALD pulses in the Al_2O_3 film. Localized charge trapping is also indicated by IPE measurements. Both changes in the slope of the Schottky and $Y^{1/2}$ plots for emission from the Al electrode in Fig. 7 appear to be correlated with the placement of the Ni impurities. Although it has been shown that IPE measurements of φ_{Bn} are relatively insensitive to charge trapped in the bulk of an insulator,[30,31] negative trapped charge in the Al_2O_3 tunnel barrier is expected to impact the onset and slope of FNT through upward band bending effects.[47] Under ideal image force barrier-lowering conditions, the slope of Schottky φ_{thresh} vs $\xi^{1/2}$ plots in Fig. 7 should be proportional to the relative optical dielectric constant, ϵ_{opt}, of the oxide. Using Eq. (3), the ϵ_{opt}s are extracted and listed in Table I. Compared to the expected value of ϵ_{opt} for Al_2O_3 of 2.5–3.0,[6] or 2.7 based on RI^2 taken from Fig. 3(b), the extracted $\epsilon_{opt} = 1.9$ for emission from the Al electrode in the *Top* device is the only one in close proximity to the expected value. All other Schottky plot slope-based values are grossly different. For emission from the TiN electrode, the high ϵ_{opt} values indicates little to no influence of image force barrier lowering and thus a sharper overall barrier. For emission from Al, the lower values are often attributed

TABLE I. Estimated optical dielectric constants, ϵ_{opt}, evaluated with the image force barrier-lowering relationship from Eq. (3) using IPE Schottky plot slopes from each electrode.

Profile	ϵ_{opt} (Al emission)	ϵ_{opt} (TiN emission)
Control	0.4	361.7
Bottom	0.6	160.8
Top	1.9	14.5

to the effect of surface dipoles or near-interfacial charging, which can alter or imitate the effect of image force barrier lowering.[30,31] Positive Al/Al_2O_3 interfacial charge in this work can be inferred from distortion near the flatband voltage for the *Control* Al_2O_3 MOS CV curve (Fig. 6) and may also be responsible for the imperfect FNT fits for the *Control* device. The positive charge at the Al/Al_2O_3 interface for the *Control* device would give rise to a rounding of the barrier due to reduction in the barrier directly at the Al/Al_2O_3 interface [Fig. 9(a)], enhancing the image force barrier-lowering effect, causing a steeper slope in the IPE Schottky plots for the Al interface.[31] With the introduction of Ni impurities, the image force barrier lowering is apparently suppressed, with the Schottky slope becoming shallower as the impurities are located closer to the Al interface. One possible explanation for the suppression of image force lowering is screening of the positive Al/Al_2O_3 interfacial charge by the negative charges associated with the Ni impurities (Fig. 9). The effect would be stronger as the negative charge centroid is moved closer to the Al interface [Fig. 9(c)], potentially explaining the reduced Schottky plot slopes [Fig. 7(c)] with the *Top* device having the shallowest slope. This negative charge, therefore, could effectively "sharpen" the barrier, giving rise to steeper IPE onset thresholds [Fig. 7(a)]. A similar type of effect has been observed after doping the near-interface region of (111) $GaAs/SrF_2$ structures with Eu.[48]

The immediate onset of symmetrically increased low-ξ leakage in all of the Al_2O_3(Ni) devices strongly suggests that the deep levels introduced into the Al_2O_3 gap by the Ni impurities lie very near to or just below the electrode Fermi levels. Not only does the energetic position of the defects in the gap symmetrically increase leakage through defect assisted conduction, negative charge associated with the Ni defects likely suppresses the onset of high-ξ FNT conduction through upward conduction band bending. The reversal and even increase of f_{asym}–ξ seen in the Al_2O_3(Ni) devices [Fig. 4(b)] and the strong dependence on Ni position demonstrate that this type of precision deep-level defect engineering is a promising approach for modifying MIM and MOS device performance. Although this work proves that intentionally introduced deep levels can be used to engineer device performance, V_{ON} is increased as a result of suppressed FNT conduction due to the Ni induced negative charge, as well as low electric field defect-enhanced conduction at both positive and negative polarity. Improving MIM device operation for energy harvesting applications will require reducing V_{ON} as well as increasing asymmetry. Reducing V_{ON} likely requires placing defect levels energetically above rather than below the electrode Fermi levels so that the defects are unoccupied and ideally uncharged, so as not to suppress the onset of FNT. In addition, placing defects above the Fermi level avoids symmetrical defect-enhanced conduction at low fields while enabling asymmetric TAT at higher biases. As schematically shown in Fig. 1, improving asymmetry will also require spatially locating defects nearer to one electrode so that they enhance TAT conduction under one bias polarity more than for the opposite polarity.

V. SUMMARY AND CONCLUSIONS

In this work, we have used ALD to precisely place transition metal Ni impurities within the insulating tunnel barrier of $TiN/Al_2O_3/Al$ MIM diodes with the intent to engineer device performance. The presence of Ni in Al_2O_3 leads to symmetric (positive and negative polarity) defect-enhanced conduction at low electric fields and the suppressed onset of FNT at negative fields without changing the relative dielectric constant, refractive index, or breakdown strength of the insulator. Current–voltage asymmetry is reversed in Al_2O_3(Ni) devices and, when Ni is placed close to the Al electrode, can even be increased. Capacitance–voltage measurements on MIM and MOS devices along with FND analysis indicate the introduction of negative charge highly correlated with the position of the ALD Ni cycles. IPE measurements indicate little change in zero-field barrier heights at the electrode interfaces and a reduced image force barrier-lowering effect at the Al/Al_2O_3 interface as Ni impurities were placed closer to the interface. These results suggest that the deep levels introduced by the Ni atoms in Al_2O_3 are consistent with DFT predictions for the corundum Al_2O_3 system and are near or slightly below equilibrium electrode Fermi levels. Although we have previously demonstrated defect-enhanced operation of MIM diodes using *intrinsic* defects as a promising approach to lowering V_{ON} and increasing f_{asym}, this work demonstrates the possibility of improving MIM diode performance using precisely placed *extrinsic* defects. It presents an opportunity to modify MIM and MOS device behavior without having to globally increase, by using processing parameters, intrinsic defect density throughout the insulator, and with greater flexibility on choice of metal electrodes, which may ease CMOS integration constraints. Introducing other transition metal impurities with different levels in the gap should provide additional ways to optimize device behavior. For example, selection of a metal that introduces deep levels above the electrode Fermi levels may lead to achievement of the low V_{ON} needed for rectenna based energy harvesting applications.

SUPPLEMENTARY MATERIAL

See the supplementary material for a cross-sectional TEM image of the doped device (Fig. S1) and time zero dielectric breakdown data for all devices (Figs. S2 and S3).

ACKNOWLEDGMENTS

The authors thank Chris Tasker of the Oregon State University for equipment support and Michael H. Hayes of the Oregon State University for developing and assisting with the RCA cleaning procedure. This work was conducted at the Materials Synthesis and Characterization (MaSC) Center, a National Nanotechnology Coordinated Infrastructure (NNCI) Northwest Nanotechnology Infrastructure (NWNI) user facility at the Oregon

State University, which is supported in part by the National Science Foundation (Grant No. NNCI-2025489) and the Oregon State University.

DATA AVAILABILITY

The data that support the findings of this study are available from the corresponding author upon reasonable request.

REFERENCES

[1]A. Thekdi and S. U. Nimbalkar, *Industrial Waste Heat Recovery—Potential Applications, Available Technologies and Crosscutting R&D Opportunities* (Oak Ridge National Lab. (ORNL), Oak Ridge, TN, 2015).
[2]T. E. Hartman, J. Appl. Phys. **33**, 3427 (1962).
[3]J. A. Bean, B. Tiwari, G. H. Bernstein, P. Fay, and W. Porod, J. Vac. Sci. Technol. B **27**, 11 (2009).
[4]Z. Thacker and P. J. Pinhero, IEEE Trans. Terahertz Sci. Technol. **6**, 414 (2016).
[5]M. N. Gadalla and A. Shamim, in *2014 44th European Microwave Conference* (IEEE, 2014), pp. 652–655.
[6]N. Alimardani, S. W. King, B. L. French, C. Tan, B. P. Lampert, and J. F. Conley, Jr., J. Appl. Phys. **116**, 024508 (2014).
[7]P. A. Schulz and C. E. T. Gonçalves da Silva, Appl. Phys. Lett. **52**, 960 (1988).
[8]S. Grover and G. Moddel, Solid-State Electron. **67**, 94 (2012).
[9]N. Alimardani and J. F. Conley, Jr., Appl. Phys. Lett. **102**, 143501 (2013).
[10]N. Alimardani and J. F. Conley, Jr., Appl. Phys. Lett. **105**, 082902 (2014).
[11]A. D. Weerakkody, N. Sedghi, I. Z. Mitrovic, H. van Zalinge, I. Nemr Noureddine, S. Hall, J. S. Wrench, P. R. Chalker, L. J. Phillips, R. Treharne, and K. Durose, Microelectron. Eng. **147**, 298 (2015).
[12]S. B. Herner, A. D. Weerakkody, A. Belkadi, and G. Moddel, Appl. Phys. Lett. **110**, 223901 (2017).
[13]E. C. Anderson, T. L. Bougher, and B. A. Cola, Adv. Electron. Mater. **4**, 1700446 (2018).
[14]I. Z. Mitrovic, A. D. Weerakkody, N. Sedghi, J. F. Ralph, S. Hall, V. R. Dhanak, Z. Luo, and S. Beeby, Appl. Phys. Lett. **112**, 012902 (2018).
[15]M. A. Jenkins, D. Z. Austin, K. E. K. Holden, D. Allman, and J. F. Conley, IEEE Trans. Electron Devices **66**, 5260 (2019).
[16]E. C. Anderson and B. A. Cola, ACS Appl. Electron. Mater. **1**, 692 (2019).
[17]W. Jeon, O. Salicio, A. Chaker, P. Gonon, and C. Vallée, IEEE Trans. Electron Devices **66**, 402 (2019).
[18]E. C. Anderson, A. P. Patel, J. J. Preston, and B. A. Cola, Nanotechnology **31**, 405202 (2020).
[19]I. Z. Mitrovic, A. D. Weerakkody, N. Sedghi, S. Hall, J. F. Ralph, J. S. Wrench, P. R. Chalker, Z. Luo, and S. Beeby, ECS Trans. **72**, 287 (2016).
[20]D. Matsuura, M. Shimizu, and H. Yugami, Sci. Rep. **9**, 19639 (2019).
[21]A. Sharma, V. Singh, T. L. Bougher, and B. A. Cola, Nat Nano **10**, 1027 (2015).
[22]J. H. Shin, J. H. Yang, S. J. Heo, and J. E. Jang, AIP Adv. **7**, 105307 (2017).
[23]K. Choi, G. Ryu, F. Yesilkoy, A. Chryssis, N. Goldsman, M. Dagenais, and M. Peckerar, J. Vac. Sci. Technol. B **28**, C6O50 (2010).
[24]J. H. Shin, J. Im, J.-W. Choi, H. S. Kim, J. I. Sohn, S. N. Cha, and J. E. Jang, Carbon **102**, 172 (2016).
[25]J. H. Yang, J. H. Shin, S. Kim, G. Pyo, A. Jang, H. W. Yang, D. J. Kang, and J. E. Jang, IEEE Electron Device Lett. **40**, 1840 (2019).
[26]M. Ichimura, J. Electron. Mater. **48**, 583 (2019).
[27]N. Alimardani, E. W. Cowell, J. F. Wager, J. F. Conley, Jr., D. R. Evans, M. Chin, S. J. Kilpatrick, and M. Dubey, J. Vac. Sci. Technol. A **30**, 01A113 (2012).
[28]K. E. K. Holden, C. L. Dezelah, and J. F. Conley, ACS Appl. Mater. Interfaces **11**, 30437 (2019).
[29]M. A. Jenkins, T. Klarr, D. Z. Austin, W. Li, N. V. Nguyen, and J. F. Conley, Jr., Phys. Status Solidi RRL **12**, 1700437 (2018).
[30]V. V. Afanas'ev, *Internal Photoemission Spectroscopy: Fundamentals and Recent Advances*, 2nd ed. (Elsevier, London, 2014).
[31]V. V. Afanas'ev and A. Stesmans, J. Appl. Phys. **102**, 081301 (2007).
[32]R. J. Powell, J. Appl. Phys. **41**, 2424 (1970).
[33]M. A. Jenkins, J. M. McGlone, J. F. Wager, and J. F. Conley, Jr., J. Appl. Phys. **125**, 055301 (2019).
[34]J. G. Baker, J. R. Schneider, J. A. Raiford, C. D. Paula, and S. F. Bent, Chem. Mater. **32**, 1925 (2020).
[35]C. Wenger, G. Lupina, M. Lukosius, O. Seifarth, H.-J. Müssig, S. Pasko, and C. Lohe, J. Appl. Phys. **103**, 104103 (2008).
[36]D. Z. Austin, D. Allman, D. Price, S. Hose, and J. F. Conley, Jr., IEEE Electron Device Lett. **36**, 496 (2015).
[37]D. Z. Austin, K. E. K. Holden, J. Hinz, and J. F. Conley, Jr., Appl. Phys. Lett. **110**, 263503 (2017).
[38]C. Besset, S. Bruyère, S. Blonkowski, S. Crémer, and E. Vincent, Microelectron. Reliab. **43**, 1237 (2003).
[39]R. Winter, J. Ahn, P. C. McIntyre, and M. Eizenberg, J. Vac. Sci. Technol. B **31**, 030604 (2013).
[40]D. Hoogeland, K. B. Jinesh, F. Roozeboom, W. F. A. Besling, M. C. M. van de Sanden, and W. M. M. Kessels, J. Appl. Phys. **106**, 114107 (2009).
[41]M. K. Matters-Kammerer, K. B. Jinesh, T. G. S. M. Rijks, F. Roozeboom, and J. H. Klootwijk, IEEE Trans. Semicond. Manuf. **25**, 247 (2012).
[42]S. Swaminathan, Y. Sun, P. Pianetta, and P. C. McIntyre, J. Appl. Phys. **110**, 094105 (2011).
[43]V. V. Afanas'ev, A. Stesmans, L. Pantisano, and T. Schram, Appl. Phys. Lett. **86**, 232902 (2005).
[44]H. B. Michaelson, J. Appl. Phys. **48**, 4729 (1977).
[45]Y.-N. Xu and W. Y. Ching, Phys. Rev. B **43**, 4461 (1991).
[46]M. L. Huang, Y. C. Chang, C. H. Chang, T. D. Lin, J. Kwo, T. B. Wu, and M. Hong, Appl. Phys. Lett. **89**, 012903 (2006).
[47]R. Kies, T. Egilsson, G. Ghibaudo, and G. Pananakakis, Appl. Phys. Lett. **68**, 3790 (1996).
[48]V. V. Afanas'ev, M. N. Mizerov, S. V. Novikov, and N. S. Sokolov, Appl. Surf. Sci. **60–61**, 637 (1992).